Electronic Journal «Technical Acoustics»
http://www.ejta.org

2007, 19

D. Bødewadt Carstensen[1*], T. Amby Christensen[1],
Morten Willatzen[1], P. V. Santos[2]

[1] *Mads Clausen Institute for Product Innovation, University of Southern Denmark, Grundtvigs Allé 150, DK-6400 Sønderborg, Denmark*
[2] *Paul-Drude-Institut für Festkörperelektronik, Hausvogteiplatz 5-7, 10117 Berlin, Germany*

Modeling of gallium arsenide surface acoustic wave devices

Received 25.06.2007, published 19.09.2007

A Surface-Acoustic Wave (SAW) device has been modeled employing a second-order Lagrangian finite-element method. The model is able to describe SAW response variations with arbitrary orientation of the unit crystal cell as compared to the macroscopic device geometry and hence allows for fast SAW design optimization. The model is used to determine the resonance frequency of different SAW device structures. The finite-element results are compared with independent analytical results obtained for two configurations of the applied electrode voltages. In order to obtain significant excitation of SAWs, it is preferable to have the electrode fingers oriented along the [110] crystal axis direction, which is the direction along the x=y line with z constant. Indeed, characteristics of normal displacement amplitudes as a function of rotation angle between the crystal axes and the electrode fingers at a fixed frequency albeit independent of the frequency verify that strong SAW excitations take place for rotation angles near 45 degrees corresponding to the [110] direction. Computations of various eigenmodes of both Rayleigh and Lamb type are discussed.

Keywords: SAW, piezoelectric, GaAs, zincblende, rotation.

INTRODUCTION

Surface acoustic waves (SAW) are elastic waves which propagate along the surface of an elastic body while dying out exponentially into the bulk of the body. SAW devices are widely used in today's modern high frequency communication systems due to their stability and reliability even in the GHz region [1]. A SAW device consists of a piezoelectric material (or film) on which interdigitated transducers (IDT) are placed. Usually a single SAW device operates as an input and an output transducer. This makes it possible to create an acoustic wave by applying a voltage signal and vice versa. This property makes SAW devices interesting for applications allowing it, e.g., to operate as an analog electric filter at selected frequencies (in the range from about 10 MHz to 2.5 GHz). SAW devices are also widely used in mobile phone technology, wireless communication and telecommunication systems [2], acoustically induced charge transport [3], light storage [4], modulation of photonic structures [5], optically cavities [6] and the driving of micromechanical systems [7, 8]. An example of more general modeling characteristics of SAW devices can be seen in the Ph. D. Thesis from A. Gantner [9].

* Corresponding author, e-mail: d_carstensen@danfoss.com

1. MODEL DESCRIPTION

A SAW-device usually consists of a piezoelectric material with several interdigitated transducers (Figure 1).

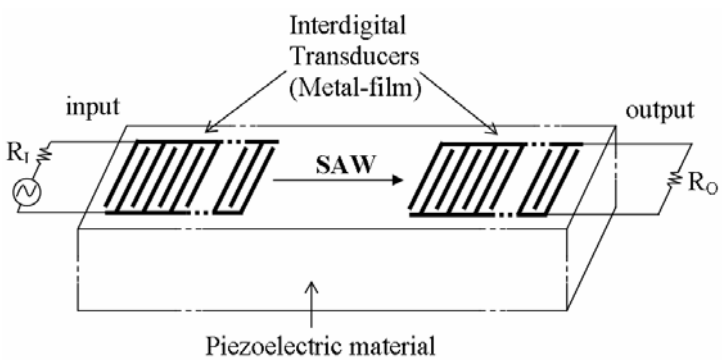

Figure 1.

SAW-device

To ease modeling, a periodic structure is assumed where only a section of the SAW-structure is modeled. Figure 2 shows a simplified piezoelectric SAW-device section of length L and height h. On the $z=h$ surface interdigitated transducers apply positive and negative voltages of equal amplitudes in an alternating manner. The piezoelectric domain is referred to as Ω_p while boundaries with positive or negative IDTs are denoted $\partial\Omega_+$ and $\partial\Omega_-$, respectively. The surface boundaries at $x=0$ and $x=L$ are referred to as $\partial\Omega_p$ while other faces are represented by $\partial\Omega_n$.

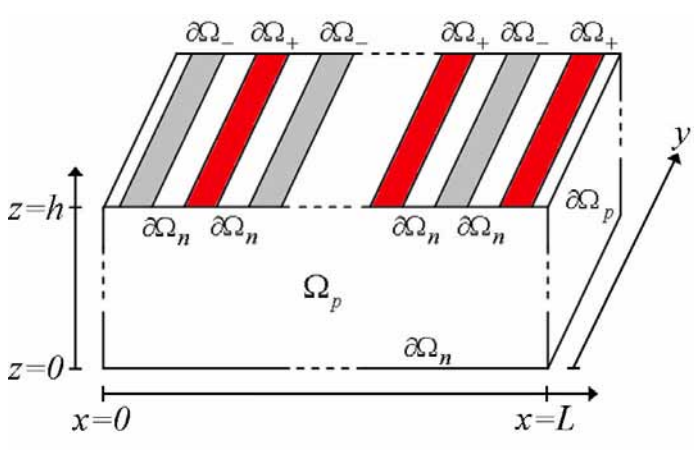

Figure 2.

Section of a SAW-device

2. MATHEMATICAL MODELING OF A SAW DEVICE

The mathematical model used in this work is based on a small segment geometry representing a section of a SAW device. The segment, treated as a 2D segment (Figure 3) as we neglect variations along the *y*-direction, consists of a piezoelectric material with IDTs mounted on the top surface. We model two types of IDT configurations, Single Finger IDTs (Figure 3a) and Double Finger IDTs (Figure 3b). The expected SAW wavelength (λ_{SAW}) is the periodic distance of the IDT electrodes. In the case of Single Finger IDTs we model a five SAW wavelength segment $L=5\lambda_{SAW}$ while in the case of Double Finger IDTs we model a one wavelength segment.

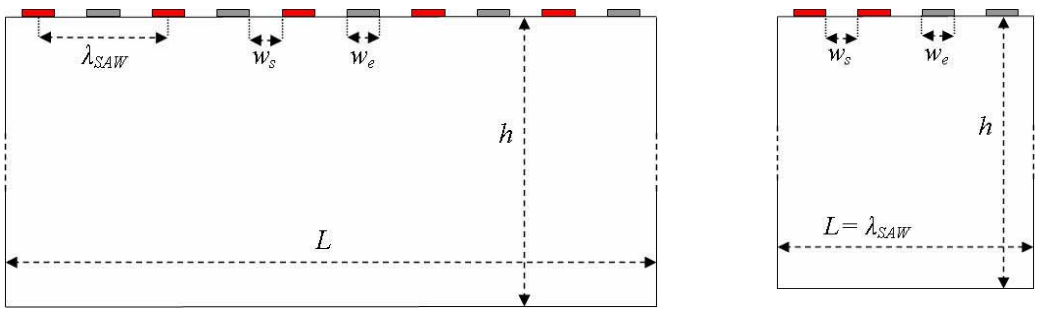

(a) Single Finger IDTs model *(b) Double Finger IDTs model*

Figure 3. 2D-section of the SAW-device

In the following we adopt the tensor notation used in [10] where subscripts *I,J,K,L* = 1,2,3,4,5,6 corresponding to *xx,yy,zz,yz,xz,xy* components, respectively, and subscripts *i,j,k,l* = 1,2,3 corresponding to *x,y,z*, respectively.

The domain Ω_p is modeled as a general piezoelectric ceramic including the coupling between mechanical and electric effects [11]. Consider the volume element *dxdydz* as shown in Figure 4 where T_{ij} is the stress component in the ith-plane along the jth-direction.

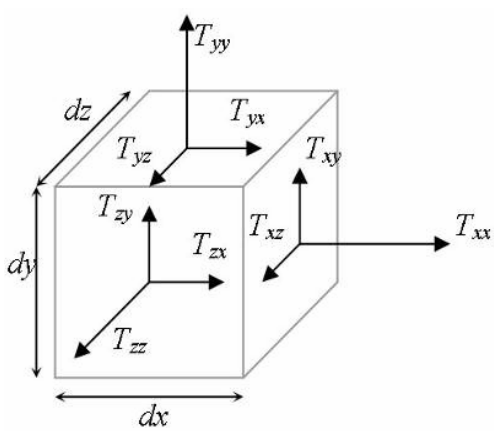

Figure 4.

Stresses on a volume element

Newton's Second Law accounts for stresses in the material due to elastic and piezoelectric contributions and can be stated as [9, 10]

$$\rho \ddot{u}_i - \frac{\partial T_{ij}}{\partial x_j} = 0, \tag{1}$$

where ρ is the mass density, $\ddot{u}_i$ is the acceleration in the ith direction, x_i is the ith spatial component.

If we next assume a monofrequency electric potential imposed at the IDE's, then — in a linear model — all other variables will be modulated at the same angular frequency. Hence, Newton's Second Law reads:

$$-\rho\omega^2 u_i - \frac{\partial T_{ij}}{\partial x_j} = 0, \tag{2}$$

where ω is the angular frequency.

Assuming no free electric charge density within the piezoelectric domain, Gauss's Law may be expressed as

$$\frac{\partial D_i}{\partial x_i} = 0, \tag{3}$$

where D_i is the electric displacement vector.

According to Faraday's Law, the electric field E_i is irrotational, when neglecting magnetic effects (not important at MHz piezoelectric applications). Thus the electric field may be defined using a scalar electric potential field:

$$E_i = -\frac{\partial V}{\partial x_i}. \tag{4}$$

2.1. Piezoelectric constitutive relations

The coupling between electrical and mechanical effects is due to the piezoelectric constitutive relations, resulting from the full free energy of the material and thermodynamic identities (setting losses in the system to zero and assuming reversibility). They read:

$$\begin{aligned} T_I &= c_{IJ}^E S_J - e_{Ij} E_j, \\ D_i &= \varepsilon_{ij}^S E_j + e_{iJ} S_J, \end{aligned} \tag{5}$$

where T, S, E, c^E, e and ε^S are the stress, strain, electric field, stiffness at constant electric field, piezoelectric stress constant, and permittivity at constant strain, respectively. Assuming small displacements the strain tensor becomes

$$S_{ji} = \mathrm{S}\left(\partial u_i / \partial x_j + \partial u_j / \partial x_i\right). \tag{6}$$

We now have a closed set of modeling equations consisting of Equation (2), (3), (4), (5) and (6), Newton's Second Law and Gauss's Law may be expressed employing mechanical displacements and the electric potential giving four equations in four unknowns: (u_i, V).

2.2. Boundary conditions

The $\partial\Omega_n$ boundaries are assumed free and insulating, thus they are modeled employing Neumann conditions. On the boundaries $\partial\Omega_+$ and $\partial\Omega_-$ the applied electric potential is modeled using a Dirichlet condition while stress components are set to zero.

The $\partial\Omega_p$ boundary is modeled as a periodic boundary condition where continuity of normal stress, normal electric displacement and tangential electric field are imposed while all mechanical displacement components are continuous.

The boundary conditions are summarized in Table 1, where V_p is the voltage amplitude of the imposed electric potential, t is the time and $i = \sqrt{-1}$.

Table 1. Boundary conditions

B.C.	Description	Expression
$\partial\Omega_+$	Applied potential No normal surface stress	$V = V_p\, exp(i\omega t)$ $n_i T_{ij} = 0$
$\partial\Omega_-$	Applied potential No normal surface stress	$V = -V_p\, exp(i\omega t)$ $n_i T_{ij} = 0$
$\partial\Omega_n$	Electric insulation No normal surface stress	$n_i D_i = 0$ $n_i T_{ij} = 0$
$\partial\Omega_p$	Continuity of normal electric displacements Continuity of tangential electric fields Continuity of normal stress Continuity of displacements	$n_i D_{i\,\|x=0} = n_i D_{i\,\|x=L}$ $V_{\|x=0} = V_{\|x=L}$ $n_i T_{ij\,\|x=0} = n_i T_{ij\,\|x=L}$ $u_{i\,\|x=0} = u_{i\,\|x=L}$

2.3. Rotation

The mathematical model is a 2D problem since, as mentioned above; we neglect variations along the y-axis, i.e. $\partial/\partial y \to 0$. Since piezoelectric materials belong to various crystal classes, the orientation of the crystal axes, relative to the geometrical shape must be defined. Usually, material parameters of piezoelectric materials are defined with respect to the crystal axes which, generally speaking, are different from the macroscopic device structure axes. Hence, it is necessary to describe how material parameter tensors must be modified so as to account for different macroscopic device directions as compared to the crystal axes of the unit cell.

If the directional vector for the geometry is given as $\vec{r}=(x,y,z)$, then the directional vector written in terms of the crystal axes, $\tilde{r}$, may be found using a coordinate transformation matrix **a**:

$$\tilde{r}_i = a_{ij} r_j \,. \tag{7}$$

When using Euler's transformation theory, the transformation matrix is defined in the Euler angles ψ, θ and ϕ rotating around x, y, and z-axis (roll-pitch-yaw) in that given order. The matrix is shown in appendix (A.3).

The rotated stiffness, piezoelectric constant and permittivity matrices may then be found using the transformation matrix and the Bond matrix **M** [10] and shown in appendix (A.4).

$$\begin{aligned} \tilde{c}_{IJ}^{E} &= M_{IK} c_{KL}^{E} M_{LJ}^{t}, \\ \tilde{e}_{iJ} &= a_{ik} e_{kL} M_{LJ}^{t}, \\ \tilde{\varepsilon}_{ij} &= a_{ik} \varepsilon_{kl} a_{lj}^{t}. \end{aligned} \tag{8}$$

The constitutive relations then take the form:

$$\begin{aligned} T_I &= \tilde{c}_{IJ} S_J - \tilde{e}_{Ij}^{t} E_j, \\ D_i &= \tilde{e}_{iJ} S_J + \tilde{\varepsilon}_{ij}^{s} E_j, \end{aligned} \tag{9}$$

which can be used to express Gauss's and Newtons's Second Law in the macroscopic geometry axes of relevance for the present problem (while quantities without tildes refer to the crystal axes). Note that superscript "*t*" denotes transpose.

3. RESULTS

In this section, we determine resonance frequencies of a GaAs SAW device for different rotation angles of the SAW device with respect to the unit cell crystal axes. The mathematical model was implemented in the finite element environment *COMSOL Multiphysics*. A Single Finger IDT SAW device as shown in Figure 3a with λ_{SAW}=2.8 µm, L=5λ_{SAW}, h=14 µm and w_s=w_e= λ_{SAW}/7=0.7 µm will be considered. Figure 5a shows a plot of the displacement u_z for different values of the rotation angle θ at a fixed frequency (rotation around the [001] crystal axis). The displacement value obtained corresponds to applying alternately +100 V and –100 V to the IDT fingers. It can clearly be seen that there exists a symmetry around the rotation angle π/4 (θ = π/4 => x=[110] direction). The Euler rotation angles and the Euler transformation matrix corresponding to a rotation to the [110] direction can be seen in appendix (A.5). At this angle and in the vicinity of it, a Rayleigh wave is generated. In actual fact, a double resonance with respect to rotation angle is found near π/4. Figure 5b shows the Rayleigh wave deformation at the top surface of the model corresponding to the rotation angle θ = π/4. Away from the symmetry point (θ = π/4) other resonance frequencies are found. The resonance frequencies near 0.632 radians and 0.939 radians (symmetric angles with respect to π/4) both correspond to Rayleigh waves. Figure 5c shows the generated Rayleigh waves at the top and bottom surface of the model. The resonance frequencies found near 0.703 radians and 0.868 radians (again symmetric angles around π/4) correspond to Rayleigh waves at the bottom surface.

We next study the model where the macroscopic structure is rotated by an angle of π/4 so as to find the SAW resonance frequencies. Sweeping the frequency from 100 MHz to 1.6 GHz

(Figure 6), a number of resonance frequencies are found. A substantial part of the other resonance frequencies (those above 1.1 GHz) correspond to Lamb waves (where strong deformations exist throughout the device and not only at the top surface). Figure 8 shows a Lamb wave deformation of the model. The resonance frequency at 1.022 GHz corresponds to a Rayleigh wave excitation, which is in excellent agreement with measurements carried out by de Lima, Jr. et al. [12, 13]. Here they examine a device with similar parameters as those used in the present work.

B. A. Auld [10] presents an analytical evaluation of surface wave velocities by solving for the velocity where symmetric and anti-symmetric Lamb waves partially cancel and create surface waves. It is argued that the surface wave velocity may be determined by the Poisson's ratio and the bulk shear wave velocity as: $v_R/v_s \approx (0.87+1.12\sigma)/(1+\sigma)$, [10, vol. 2, eq. 10.35] where v_R , v_s and σ are the surface wave velocity, bulk shear wave velocity, and the Poisson ratio, respectively. The Poisson ratio is determined from the stiffness along the bulk longitudinal (x) direction and the bulk shear (z) direction. Accordingly, for the problem with a rotated unit-cell crystal as compared with the SAW-device axes, the rotated stiffness values must be used. Employing equation (8) with a rotation angle $\theta = \pi/4$, the bulk longitudinal and bulk shear stiffness become: $\tilde{c}_{11}^E = (c_{11}^E + c_{12}^E + 2c_{44}^E)/2$ and $\tilde{c}_{13}^E = c_{13}^E$, respectively. Hence, the Poisson ratio is $\sigma = (\tfrac{1}{2} - \tilde{c}_{13}^E/\tilde{c}_{11}^E)/(1-\tilde{c}_{13}^E/\tilde{c}_{11}^E)$. Given the material constants of GaAs (listed in the Appendix), the Poission ration becomes $\sigma = 0.2111$. The bulk shear velocity for the structure now reads: $v_s = \sqrt{\tilde{c}_{13}^E/\rho} = 3163$ m/s. Using the approximation in [10], the surface wave velocity is estimated to $v_R = 2890$ m/s. We expect the first surface wave resonance frequency occurs when the wavelength matches the shortest distance between two electrodes having the same applied potential (denoted as λ_{SAW} in Figure (3a)). Thus, by analytic evaluation, the first surface wave resonance frequency is expected at $f_0 = v_R/\lambda_{SAW} = 1.032$ GHz when $v_R = 2890$ m/s and the periodic electrode distance is $\lambda_{SAW} = 2.8$ µm. The analytical work presented in [10] agrees too within 1% of the present work based on the finite element method and the experimental result by Lima, Jr. et al. [12, 13].

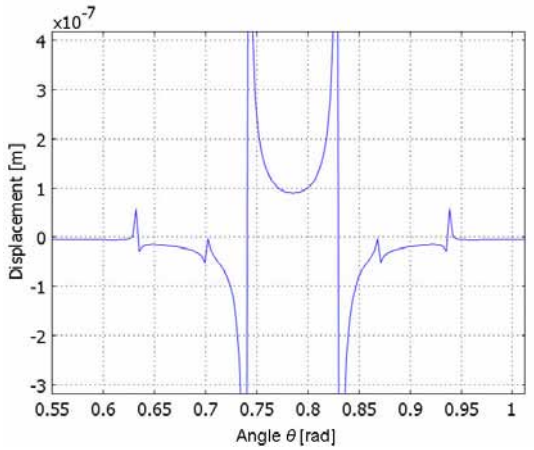

Figure 5a.

Angle sweep – at constant frequency 1.022 GHz (u_z displacement). The displacement value obtained corresponds to applying alternately +100 V and –100 V to the IDT fingers

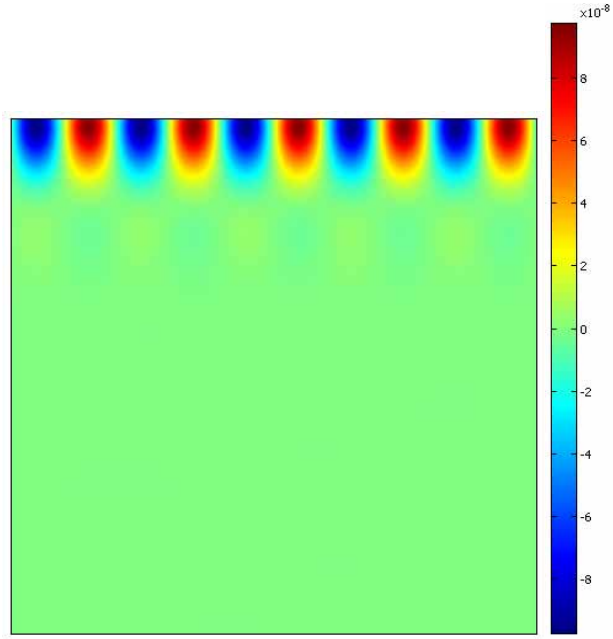

Figure 5b.

Rayleigh wave at the top surface $\theta = \pi/4$ radians, frequency=1.022 GHz (u_z displacement)

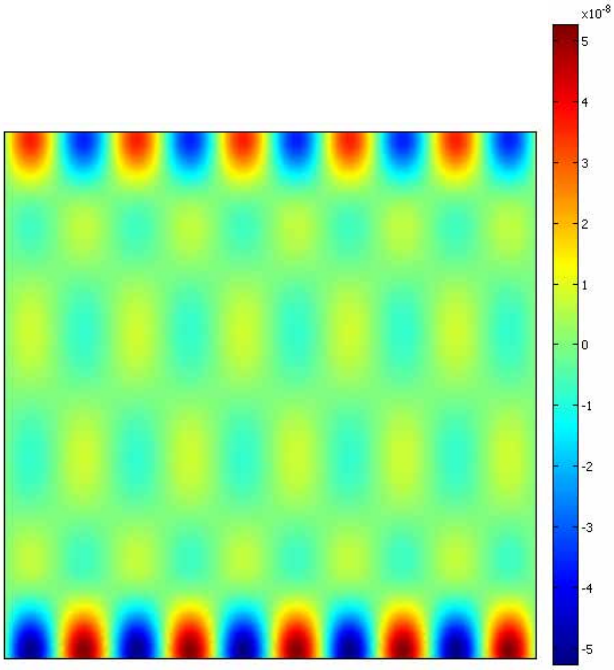

Figure 5c.

Rayleigh wave at the top and bottom surfaces $\theta = 0.632$ radians or $\theta = 0.939$ radians, frequency=1.022 GHz (u_z displacement)

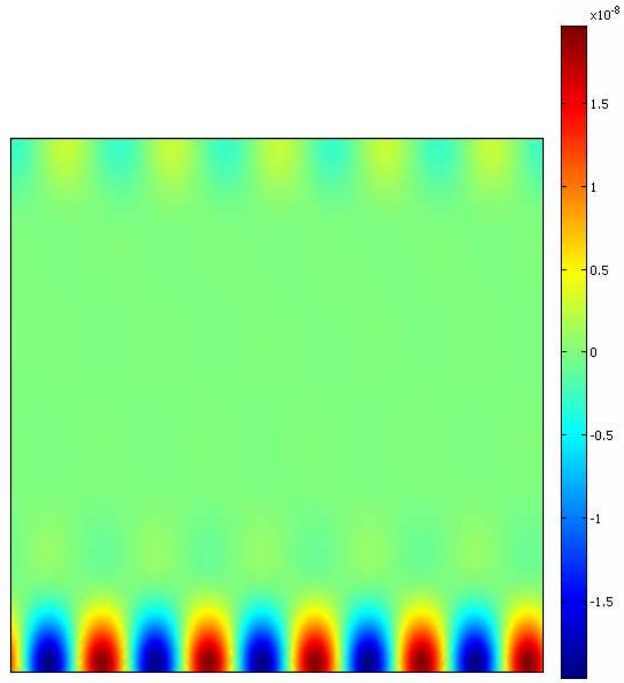

Figure 5d.

Rayleigh wave at the bottom surface $\theta = 0.703$ radians or $\theta = 0.868$ radians, frequency=1.022 GHz (u_z displacement)

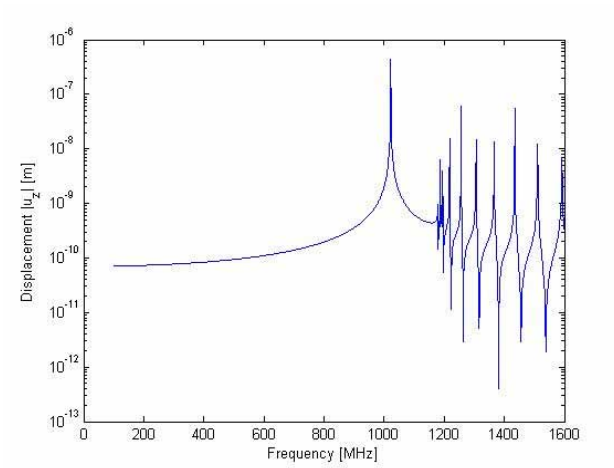

Figure 6.

Frequency sweep – fixed angle $\theta = \pi/4$ radians ($|u_z|$ displacement). The displacement value obtained corresponds to applying alternately +100 V and –100 V to the Single Finger IDTs

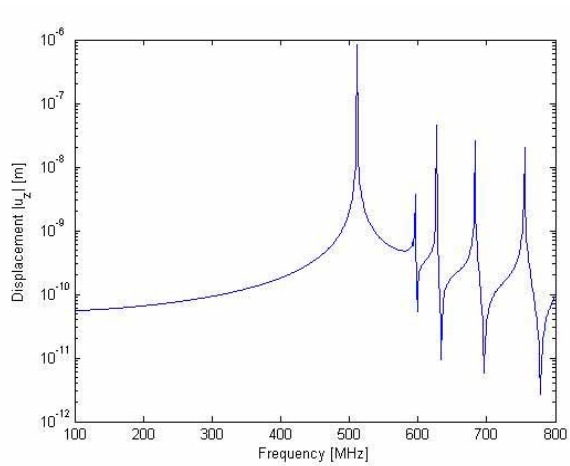

Figure 7.

Frequency sweep – fixed angle $\theta = \pi/4$ radians ($|u_z|$ displacement). The displacement value obtained corresponds to applying alternately +100 V and –100 V to the Double Finger IDTs

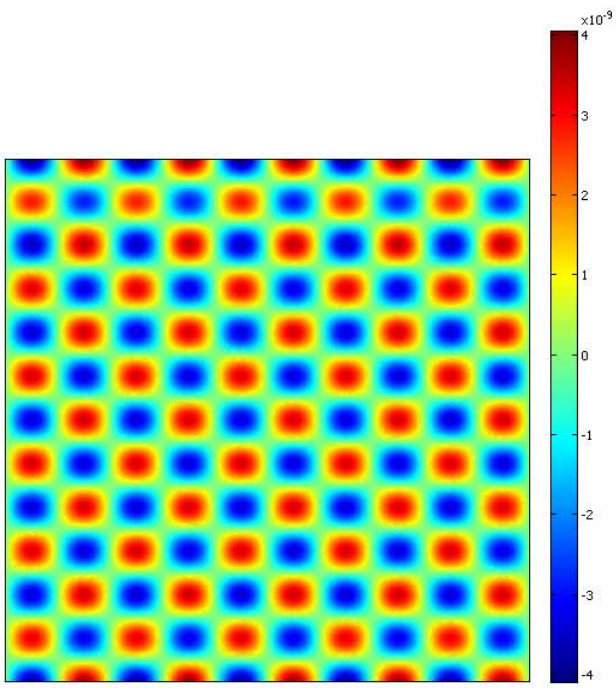

Figure 8.

Lamb wave, frequency = 1.512 GHz and angle $\theta = \pi/4$ radians (u_z displacement)

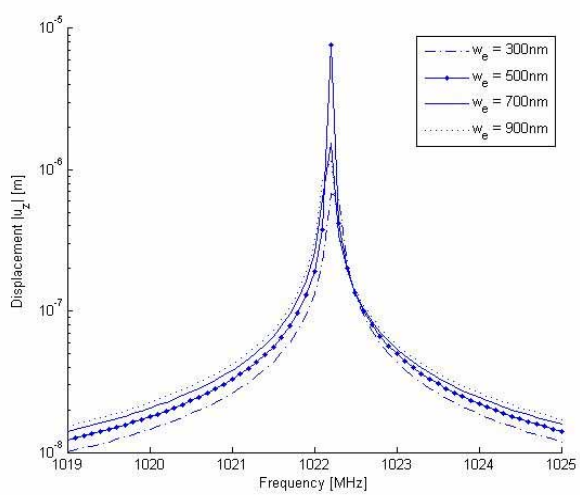

Figure 9.

SAW resonance frequency for Single Finger IDTs with varying finger/electrode width

Next, we study a Double Finger IDT SAW device with λ_{SAW} = 5.6μm, $L = \lambda_{SAW}$, h = 14 μm and $w_s = w_e$ = 0.7 μm. As above the macroscopic device geometry is rotated by an angle of π/4 with respect to the crystal unit cell (GaAs). Also here we apply + 100V and –100 V to the IDTs alternatingly, but now the IDT configuration is set up such that the applied potential changes sign in steps of two neighboring fingers (refer to Figure 3b). As expected, and in agreement with [12, 13], the SAW resonance frequency is found near 510 MHz being half of the SAW resonance frequency found for the Single Finger IDT configuration (with a SAW wavelength λ_{SAW} = 2.8 μm). Figure 7 shows $|u_z|$ for a frequency sweep between 100 MHz to 800 MHz. A substantial part of the other resonance frequencies found (those above 590 MHz) correspond to Lamb waves.

Using the Single Finger IDT configuration again we next study the influence of the width of IDT fingers/electrodes with respect to the SAW frequency band. Figure 9 shows the resonance frequency for four models only differing in the finger/electrode width used (w_e = 0.3 μm, w_e = 0.5 μm, w_e = 0.7 μm and w_e = 0.9 μm). Comparing the four graphs it is observed that the influence of the finger width is rather weak. The SAW frequency band becomes a bit narrower when the finger/electrode width is reduced. Obviously, near the resonance peaks, losses must be accounted for in determining actual displacement values.

The model implemented does not include damping terms. Damping effects are usually complicated. However, viscoelastic effects accounting partially for acoustic losses in materials can be easily introduced in the modeling equations by including a strain derivative term with respect to time: $T_I = c^E_{IJ} S_J + \eta_{IJ}\, \partial S_J / \partial t - e_{Ij} E_j$ where η_{IJ} is a 6×6 viscosity matrix. It is known [10, Chap. 7] that the viscosity tensor takes the same general form as the stiffness tensor and hence transforms similar to the stiffness matrix, i.e. $\tilde{\eta}_{IJ} = M_{IK} \eta_{KL} M^t_{LJ}$.

4. CONCLUSIONS

Our theoretical model is used to investigate SAW devices based on a GaAs zincblende crystal. In the case where the IDT fingers are aligned with the crystal axes, electrical excitation is not possible. However, rotating the rectangular structure such that IDTs are tilted with respect to crystal axes, it becomes possible to generate surface acoustic waves. It is shown for such a structure that an angular resonance exists around π/4. Scanning in frequency the rotated structure (with rotation angle θ = π/4) gives a frequency resonance near 1.022 GHz (corresponding to finger width and interspacing equal to 0.7 micrometer) in excellent agreement with experimentally obtained values. The proposed model makes it possible to optimize SAW device geometries for arbitrary unit-cell crystal class and orientation.

REFERENCES

1. C. C. W. Ruppel and T. A. Fjeldly. Advances in Surface Acoustic Wave Technology, Systems and Applications-1. Selected Topics in Electronics and Systems, World Scientific, 19 (2000).
2. C. K. Campbell. Surface Acoustic Wave Devices for Mobile and Wireless Communications. Applications of Modern Acoustics, Academic Press (1998).
3. M. J. Hoskins, H. Morkoç and B. J. Hunsinger. Surface acoustic wave on the (112) cut [110] direction of gallium arsenide. Appl. Phys. Lett., 41, 332 (1982).
4. C. Rocke, S. Zimmermann, A. Wixforth, J. P. Kotthaus, G. Böhm and G. Weimann. Acoustically Driven Storage of Light in a Quantum Well. Phys. Rev. Lett., 78, 4099 (1997).
5. P. V. Santos. Collinear light modulation by surface acoustic waves in laterally structured semiconductors. Journal of Applied Physic, 89, 5060 (2001).
6. M. M. de Lima, Jr., R. Hey and P. V. Santos. Appl. Phys. Lett., 83, 2997 (2003).
7. F. W. Beil, A. Wixforth and R. H. Blick. Active photonic crystals based on surface acoustic waves. Physica E (Amsterdam), 13, 473 (2002).
8. Y. Takagaki, E. Wiebicke, P. V. Santos, R. Hey and K. H. Ploog. Propagation of surface acoustic waves in a GaAs/AlAs/GaAs heterostructure and micro-beams. Semicond. Sci. Technol., 17, 1008 (2002).
9. A. Gantner, Mathematical modeling and numerical simulation of piezoelectrical agitated surface acoustic waves. Ph.D. Thesis. Faculty of Mathematics and Natural Sciences, University of Augsburg, Germany (2005).
10. B. A. Auld. Acoustic Fields and Waves in Solids, vol. 1 and 2, 2nd edition. Krieger Publishing Company (1990).
11. M. Willatzen. Ultrasound transducer modeling – general theory and applications to ultrasound reciprocal systems. IEEE Transactions on Ultrasonics, Ferroelectrics, and Frequency Control, 48, 100–112 (2001).
12. M. M. de Lima, Jr., W. Seidel, H. Kostial and P. V. Santos. Embedded interdigital transducers for high-frequency surface acoustic waves on GaAs. Journal of Applied Physic, 96, 3494–3500 (2004).
13. M. M. de Lima, Jr., W. Seidel, F. Alsina and P. V. Santos. Focusing of surface-acoustic-wave fields on [100] GaAs surfaces. Journal of Applied Physics. 94, 7848–7855 (2003).

APPENDIX

The stiffness tensor at constant electric field- , the piezoelectric stress tensor and the permittivity tensor at constant strain read:

$$\mathbf{c}^E = \begin{pmatrix} c_{11}^E & c_{12}^E & c_{13}^E & c_{14}^E & c_{15}^E & c_{16}^E \\ c_{21}^E & c_{22}^E & c_{23}^E & c_{24}^E & c_{25}^E & c_{26}^E \\ c_{31}^E & c_{32}^E & c_{33}^E & c_{34}^E & c_{35}^E & c_{36}^E \\ c_{41}^E & c_{42}^E & c_{43}^E & c_{44}^E & c_{45}^E & c_{46}^E \\ c_{51}^E & c_{52}^E & c_{53}^E & c_{54}^E & c_{55}^E & c_{56}^E \\ c_{61}^E & c_{62}^E & c_{63}^E & c_{64}^E & c_{64}^E & c_{66}^E \end{pmatrix},$$

$$\mathbf{e} = \begin{pmatrix} e_{11} & e_{12} & e_{13} & e_{14} & e_{15} & e_{16} \\ e_{21} & e_{22} & e_{23} & e_{24} & e_{25} & e_{26} \\ e_{31} & e_{32} & e_{33} & e_{34} & e_{35} & e_{36} \end{pmatrix}, \tag{A.1}$$

$$\boldsymbol{\varepsilon}^S = \begin{pmatrix} \varepsilon_{11}^S & \varepsilon_{12}^S & \varepsilon_{13}^S \\ \varepsilon_{21}^S & \varepsilon_{22}^S & \varepsilon_{23}^S \\ \varepsilon_{31}^S & \varepsilon_{32}^S & \varepsilon_{33}^S \end{pmatrix}.$$

Material constants for GaAs piezoelectric Zincblende $\bar{4}3\mathrm{m}$ crystals (inversion-asymmetric cubic) are [10]:

$$\mathbf{c}^E = \begin{pmatrix} 11.83 & 5.32 & 5.32 & 0 & 0 & 0 \\ 5.32 & 11.83 & 5.32 & 0 & 0 & 0 \\ 5.32 & 5.32 & 11.83 & 0 & 0 & 0 \\ 0 & 0 & 0 & 5.95 & 0 & 0 \\ 0 & 0 & 0 & 0 & 5.95 & 0 \\ 0 & 0 & 0 & 0 & 0 & 5.95 \end{pmatrix} \left[\frac{10^{10}\,N}{m^2}\right],$$

$$\mathbf{e} = \begin{pmatrix} 0 & 0 & 0 & 0.16 & 0 & 0 \\ 0 & 0 & 0 & 0 & 0.16 & 0 \\ 0 & 0 & 0 & 0 & 0 & 0.16 \end{pmatrix} \left[\frac{C}{m^2}\right], \quad \frac{\varepsilon_r^S}{\varepsilon_0} = \begin{pmatrix} 12.45 & 0 & 0 \\ 0 & 12.45 & 0 \\ 0 & 0 & 12.45 \end{pmatrix}, \tag{A.2}$$

ρ = 5316 [kg/m^3].

The Euler coordinate transformation matrix (roll-pitch-yaw convention) obtained by rotation about the *z*, *y* and *x*-axis (in the given order) reads:

$$\mathbf{a} = \begin{pmatrix} a_{xx} & a_{xy} & a_{xz} \\ a_{yx} & a_{yy} & a_{yz} \\ a_{zx} & a_{zy} & a_{zz} \end{pmatrix} = \begin{pmatrix} \cos(\phi)\cos(\theta) & \sin(\phi)\cos(\theta) & -\sin(\theta) \\ \cos(\phi)\sin(\theta)\sin(\psi) - \sin(\phi)\cos(\psi) & \cos(\phi)\cos(\psi) + \sin(\phi)\sin(\theta)\sin(\psi) & \cos(\theta)\sin(\psi) \\ \cos(\phi)\sin(\theta)\cos(\psi) + \sin(\phi)\sin(\psi) & \sin(\phi)\sin(\theta)\cos(\psi) - \cos(\phi)\sin(\psi) & \cos(\theta)\cos(\psi) \end{pmatrix}. \tag{A.3}$$

The Bond matrix given in ref. [10] referring to (A.3) is

$$\mathbf{M} = \begin{pmatrix} a_{xx}^2 & a_{xy}^2 & a_{xz}^2 & 2a_{xy}a_{xz} & 2a_{xz}a_{xx} & 2a_{xx}a_{xy} \\ a_{yx}^2 & a_{yy}^2 & a_{yz}^2 & 2a_{yy}a_{yz} & 2a_{yz}a_{yx} & 2a_{yx}a_{yy} \\ a_{zx}^2 & a_{zy}^2 & a_{zz}^2 & 2a_{zy}a_{zz} & 2a_{zz}a_{zx} & 2a_{zx}a_{zy} \\ a_{yz}a_{zx} & a_{yy}a_{zy} & a_{yz}a_{zz} & a_{yy}a_{xx} + a_{yz}a_{zy} & a_{yx}a_{zz} + a_{yz}a_{zx} & a_{yy}a_{zx} + a_{yx}a_{zy} \\ a_{zx}a_{xx} & a_{zy}a_{xy} & a_{zz}a_{xz} & a_{xy}a_{zz} + a_{xz}a_{zy} & a_{xz}a_{zx} + a_{xx}a_{zz} & a_{xx}a_{zy} + a_{xy}a_{zx} \\ a_{xx}a_{yx} & a_{xy}a_{yy} & a_{xz}a_{yz} & a_{xy}a_{yz} + a_{xz}a_{yy} & a_{xz}a_{yx} + a_{xx}a_{yz} & a_{xx}a_{yy} + a_{xy}a_{yx} \end{pmatrix}. \tag{A.4}$$

As an example, the Euler rotation angles and the Euler coordinate transformation matrix for a transformation to the [110] direction becomes

$$\left(\psi = 0\ ,\ \phi = 0\ ,\ \theta = \frac{\pi}{4}\right) \Rightarrow \quad \mathbf{a} = \begin{pmatrix} \frac{1}{\sqrt{2}} & \frac{1}{\sqrt{2}} & 0 \\ -\frac{1}{\sqrt{2}} & \frac{1}{\sqrt{2}} & 0 \\ 0 & 0 & 1 \end{pmatrix} \tag{A.5}$$